

## PORE SCALE ANALYSIS OF ELECTRICAL RESISTIVITY IN COMPLEX CORE MATERIAL

M. A. Knackstedt<sup>1,2</sup>, C. H. Arns<sup>1</sup>, A. P. Sheppard<sup>1</sup>, T. J. Senden<sup>1</sup>, R. M. Sok<sup>1</sup>, Y. Cinar<sup>2</sup>,  
A. O. Olafuyi<sup>2</sup>, W. V. Pinczewski<sup>2</sup>, G. Padhy<sup>3</sup>, M. Ioannidis<sup>3</sup>

(1) Applied Maths, RSPHysSE, Australian National University, Canberra, Australia

(2) School of Petroleum Engineering, University of New South Wales, Sydney, Australia

(3) Chemical Engineering, University of Waterloo, Toronto, Canada

*This paper was prepared for presentation at the International Symposium of the  
Society of Core Analysts held in Calgary, Canada, 10-12 September, 2007*

### ABSTRACT

This paper presents results of a 3D pore scale study of the resistivity properties in twelve model and reservoir core samples. Samples include sintered bead packs, homogeneous consolidated sandstones, thinly bedded sands, sucrosic dolomites, dual porosity samples and heterogeneous carbonate core material. Predictions of Archie's cementation exponent  $m$  and saturation exponent  $n$  (under well defined wettability conditions) are in good agreement with experiment where available. We note a consistent increase in  $m$  with decreasing porosity in sandstones. The value of  $m$  in carbonates may be empirically related to the fraction of disconnected macroporosity. Under water wet conditions the simple clastic and carbonate samples exhibit Archie-type behaviour. The laminated sand exhibit strong anisotropy and the complex carbonate systems exhibit values of  $n$  that vary strongly with water saturation. Large values of  $n > 4$  are observed under idealized oil wet conditions. Pore and fluid phase connectivity is examined for the image data and used to explain trends observed in the data.

### INTRODUCTION

Relating the hydrocarbon saturation of reservoir rocks to their bulk electrical conductivity is among the most fundamental problems in petrophysics and core/log analysis. The empirical relation between resistivity, porosity and hydrocarbon saturation was first noted by Archie and remains the main tool for saturation estimates from resistivity measurements. Conventionally, values are assumed to be  $m = n = 2$ . Significant scatter in laboratory measured data for  $m$  and  $n$  from complex lithologies have been noted and petrophysicists suspect that the major cause of the discrepancy is due to rock heterogeneity and the complicated pore structure in complex lithologies. Pore network simulations are established tools for the simulation of two-phase fluid flow in porous materials and have been widely used to determine electrical resistivity (Blunt et al. 2002, Man and Jing 2002, Bekri 2003 and references therein) in reservoir core samples with complex pore structures. In network models the advancement of the fluid-fluid interface is governed by capillary pressure, wettability and a, necessarily, simplified local channel cross-section geometry. For certain wettability conditions, direct *image-based* pore scale

simulation of electrical properties on 3D image data has been described (Toumelin et al., 2006). To date this has been limited to simple packs which do not reflect the heterogeneity in many complex reservoir cores.

This paper presents the results of an integrated experimental and direct 3D image-based pore scale study of the relationship between Archie's  $m$  and  $n$  values and pore structure in complex lithologies. We carry out 3D pore scale imaging and electrical resistivity index measurements during drainage on a large suite of complex core material including homogeneous and heterogeneous reservoir sandstones, synthetic vuggy porous media and carbonate reservoir core material. Prediction of  $m$  and  $n$  parameters from the image data are compared to available laboratory based measurements and found to be in agreement. We observe a strong variation of  $n$  in the thinly bedded samples parallel and perpendicular to the bedding planes. We also observe a strong variation in  $m$  and  $n$  for different carbonate systems. The exponent  $n$  is found to vary strongly with saturation. We consider the relative interconnectivity and tortuosity of pores in the different complex lithologies and their contribution to the electrical transport. This pore scale quantification aids in explaining the scatter observed in  $m$  and  $n$  for complex pore geometries.

## **METHODS**

### Samples, Imaging and Experiment

Twelve samples are considered in this paper. Samples included a monodisperse glass bead pack, three Fontainebleau sandstone samples, a clean Aeolian sandstone exhibiting fine scale laminations at the mm scale (Ghous et al., 2005), four sucrosic dolomites, one model dual porosity carbonate (Padhy et al., 2005, 2006) and two heterogeneous bioclastic grain/packstone from Abu Dhabi (Sok et al., 2007). Images of the samples were obtained at the ANU micro-CT facility (Sakellariou et al., 2004, 2004a) at resolutions down to 2.85 microns per voxel. All images were composed of  $2048^3$  voxels. Examples of images are given in Fig. 1 and descriptions and porosities of the samples measured via porosimetry and derived from the image data is summarized in Table 1.

In Samples 1-10 the attenuation histogram exhibits multimodal distributions allowing unambiguous phase separation (Sheppard et al., 2004) of the pore phase from the mineral phase (Fig. 2(a-b)). In all cases the resolvable porosity is compared to experiment with good agreement. In samples 11-12 the presence of pores below image resolution required the assignment of microporosity ( $\phi_{\text{micro}}$ ) from image data. Inclusion of the microporous contribution to porosity can be made based on attenuation of the tomogram (for details of method see Sok et al., 2007). This leads to reasonable agreement with experiment. One can also partition the resolved porosity into macroscopically connected macroporosity and macropores connected only via the microporous phase (Fig. 2(c-d)). These porosities are reported in Table 1. In all cases the quality of the image is directly tested by comparing experimental measurement of pore throat size via MICP to simulations of MICP (Knackstedt et al., 2006; Sok et al., 2007); the agreement is good in all samples.

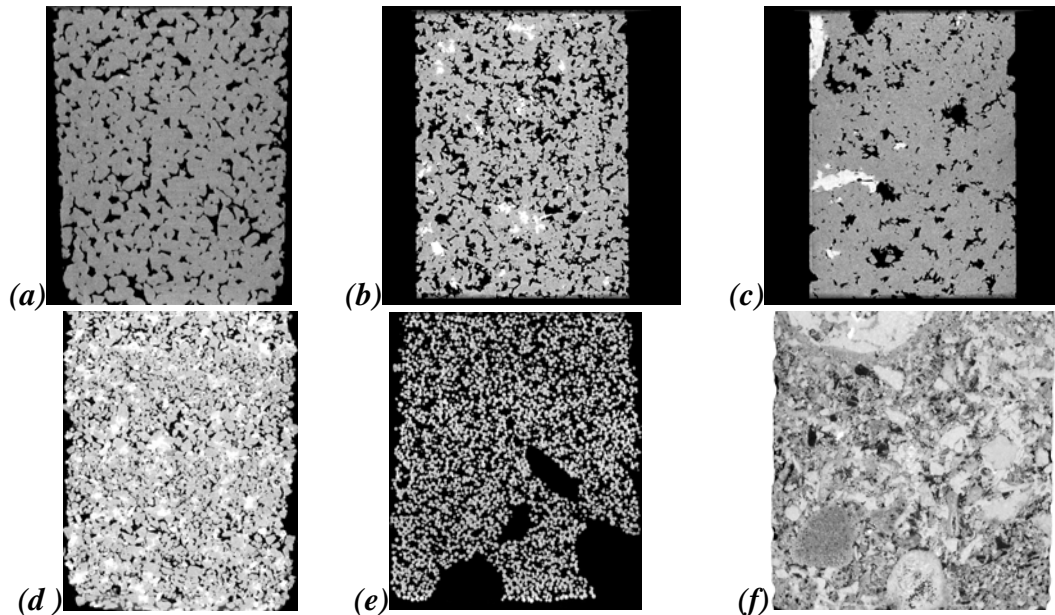


**Figure 1:** Examples of 2D slices through 3D grey scale tomographic images of rock samples used in this study. (a) Fontainebleau sand, (b), (c) sucrosic dolomite, (d) Aeolian sand, (e) artificial vuggy carbonate and (f) complex carbonate. Image sizes are 2000 x voxel size given in Table 1.

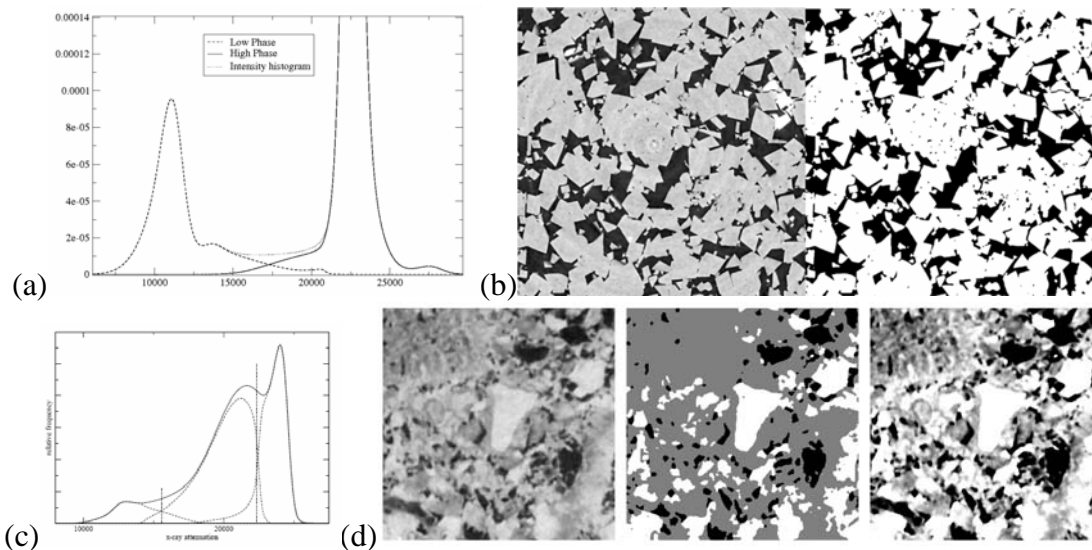


**Figure 2:** (a) Typical x-ray attenuation distribution obtained on clean samples 1-10. This allows unambiguous phase separation of sample in (b); Image size =  $(1.425 \text{ mm})^2$ . (c) Samples 11-12 exhibit a range of attenuation with peaks associated with pore and solid calcite phase evident. The intermediate attenuation region is identified as meso/microporous. (d) shows the original image (left). The middle image gives the resultant three phase partition (white solid, black pore, grey microporous). The right figure shows the microporous phase with the original attenuation, used to assign porosity in the phase; Image size =  $(1.14 \text{ mm})^2$ .

**Table 1.** Description and experimental/image porosities of samples studied. In 10 cases the porosity was measured on the same core material. In two cases (\*) the porosity was measured on sister core material. For the reservoir carbonates we report the resolved porosity from the image, the resolved and macroscopically connected porosity and the porosity after inclusion of the microporous fraction. Indicative permeabilities for the samples are also shown.

Sample	Samples	Voxel Size	$\phi_{\text{exp}}(\%)$	$\phi_{\text{image}}(\%)$	k (mD)
1	Bead Pack	55	25.8	27.2	>10000
2-4	Fontainebleau	2.85	6.8/13.1 / 17.4	7.7/13.2 / 17.8	10-500
5	Aeolian Sand	4.2	21.8*	18.4	30 (Perp to bedding) 300 (Parallel)
6-9	Dolomite	2.85	12.8 / 18.6 / 19.1 / 27.9	12.0 / 18.1 / 19.5 / 28.3	200-3500
10	Artificial Vuggy	5.0	46.8*	54.7	4000
11-12	Reservoir Carbonates	2.85	28.9 / 26.7	Resolved: 17.0/10.8 Connected: 8.8/1.7 Total: 27.1 / 23.2	20-100 mD

### Computational Methods

We use a finite-element method (FEM) to estimate the electrical conductivity of the image data (Garboczi & Day, 1995, Arns 2002). FEM uses a variational formulation of the linear conductivity equations and solves Laplace equation by minimizing the energy using a fast conjugate-gradient method. Each voxel is taken to be a trilinear finite element. Non-periodic boundary conditions are used and calculations carried out for voltage gradients applied along each of the major tomogram axes, giving three principal conductivities defined by the tomogram axes. The parallel solver scales linearly to system sizes well above  $1000^3$  voxels (tested for 256 processors). For the resistivity calculations we assign zero conductivity ( $\sigma=0$ ) to the solid and oil phases and  $\sigma=1$  to the water phase.

We consider two simple extremes of wettability; strongly oil-wet and strongly water-wet. The fluid geometries are distributed assuming the fluids have migrated and occupy the most favourable pore spaces; for the water wet case the oil will fill the largest pores and throats while the water will preferentially occupy the smaller pores and throats. In the oil-wet case the fluid distributions are reversed; oil will now preferentially occupy the smaller pores and throats. This case is equivalent to laboratory cores which have been treated by a wettability altering agent (see e.g, Sharma et al., 1991). To define the phase distribution at different saturations and under varying wetting conditions we define locally on the image the diameter of the largest sphere which lies within the pore space and covers every voxel. Non wetting fluid resides in the regions of large covering sphere radius and the wetting fluid resides in regions with small covering radius. By incrementing the value of the covering sphere radius one can vary the effective saturation. An illustration of the fluid distributions within a small subset of an unconsolidated sample volume under water-wet conditions at high and low water saturations is shown in 2D in Fig. 3. Different fluid distribution scenarios are considered (Toumelin et al., 2006). Drainage of a water-wet rock model is simulated via propagation

of the non-wetting phase from the periphery of the core inwards. Imbibition is simulated via film thickening of the non-wetting fluid in regions of small radius (high capillary pressure). A more comprehensive study of various wetting scenarios and displacement processes (see e.g. Man & Jing, 2002) are beyond the scope of the present study.

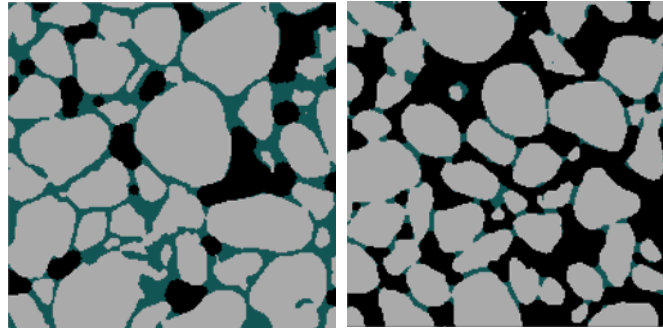


**Figure 3:** Illustration in 2D of wetting phase distribution (blue) within the pore space (black) of a poorly consolidated sand sample. (a) is a snapshot at higher (55%) water phase saturation and (b) at low (near irreducible, ~15%) water saturation; Image size =  $(400)^2$  voxels.

## RESULTS

### Sintered Bead Pack

The value of  $m$  derived from the image data of a monodisperse sintered bead pack along three orthogonal axes is  $m=1.40, 1.41$  and  $1.42$ . This result is in excellent agreement with experimental and model data obtained previously on sintered glass bead packs; in particular (Sharma, 1991) performed a number of experiments on lightly sintered glass bead packs and obtained a value of  $m=1.39 \pm .1$ .

RI results are summarized in Fig. 4(a). The best fit to the water wet drainage data is  $n=2.04$ . This is again in agreement with experimental data on sintered glass beads from (Sharma et al., 1991) who reported  $2.22 \pm .3$ . The oil wet samples exhibit a much higher value of  $n>5$  for all saturations with  $n$  increasing with decreasing  $S_w$ . This strong difference in  $n$  under different wettability conditions mirrors the data of (Sharma et al., 1991) who found that  $n=4.84 \pm 1.6$ .

### Fontainebleau Sandstone

The data for the cementation exponent of the three Fontainebleau sandstone samples is given in Fig. 5(a). Calculations were performed on two  $(960)^3$  subsamples of the image and measured in three orthogonal directions (six data points per sample). Comparison with experimental data for Fontainebleau is shown. For the higher porosity samples we observe a consistent value of  $m$  and a significant increase in  $m$  at lower porosities. This is in agreement with experimental data which exhibits an increase of  $m$  for  $\phi<10\%$ . The simulated data for water wet drainage into the two higher porosity Fontainebleau sandstone samples is given in Fig. 4(b)-(c). Experimental porous plate RI measurements are undertaken in our laboratories on sister plugs of both samples for comparison. In all

cases we observe a good match between simulation and experiment with classic Archie behaviour,  $n=2$  for all  $S_w > 0.2$ . At lower saturations the value of  $n$  in the simulations increases; this is not observed experimentally. We believe this variation at low saturations may be due to the lack of continuity in the films at low saturations in the image data; in experiments continuous films will be present in some pores at length scales below image resolution. We also simulate RI under oil wet conditions and observe very different  $n$  values under oil wet conditions;  $n > 5$  for all saturations (data not shown).

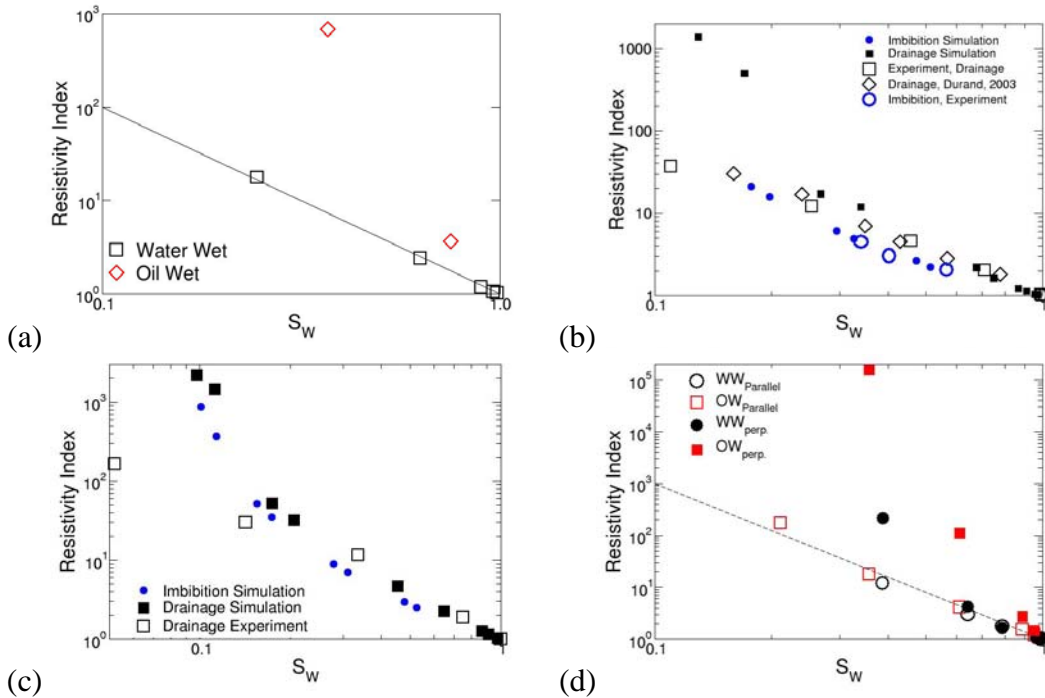


**Figure 4:** RI vs.  $S_w$  for sandstones; (a) sintered bead pack. (b-c) show RI data for the two higher porosity Fontainebleau samples; (b) gives the Fontainebleau data for the sample at  $\phi=13\%$  and (c) the data for the the sample at  $\phi=17\%$ . The data for drainage into the Aeolian sand is shown in (d). WW refers to water wet conditions and OW to oil-wet conditions. Parallel and perpendicular indicate orientation vs bedding planes.

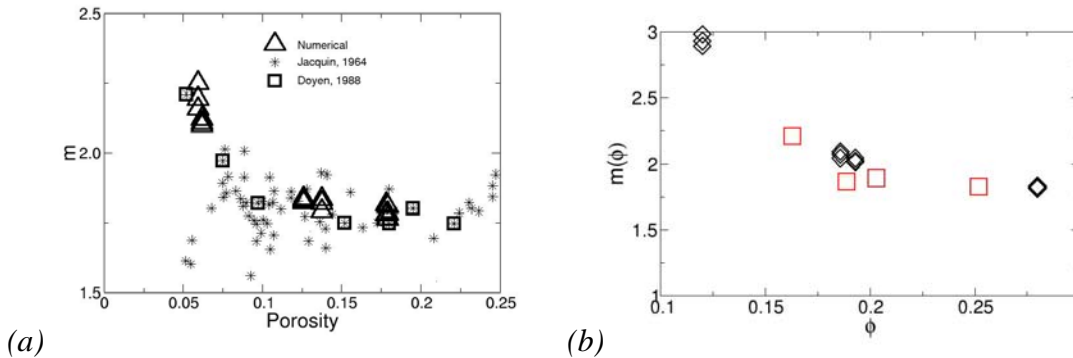


**Figure 5:** Archie's cementation exponent as a function of saturation for (a) Fontainebleau samples and (b) homogeneous dolomite samples.

### Aeolian Sandstone

Simulation of resistivity under water saturated conditions exhibits only a small anisotropy in the cementation exponent; parallel to the bedding planes  $m=1.77$  and perpendicular to the bedding planes  $m=1.96$ . We then consider the saturation exponent of the clean laminated sample. Very strong anisotropy is observed in Fig. 4(d). Under water wet conditions we observe  $n=2.7$  parallel to the bedding plane. Perpendicular to the bedding planes we observe a highly non-linear trend and  $n>5$  at intermediate saturations. Parallel to the bedding plane the saturation exponent under oil wet conditions gives  $n\sim 3$ ; a very low value for  $n$  under oil wet conditions and very similar to the value obtained for water wet conditions. The value perpendicular to the bedding plane under idealised oil-wet conditions exhibits very large values of  $n>10$ .

The similar values of  $n$  parallel to the bedding plane under oil-wet and water-wet conditions may be understood by visualising the phase distribution within the image data. An example of the phase distributions within the sample in 2D at  $S_w = 0.42$  is shown in Fig. 6(a). The pores in the tighter laminations remain largely fully water saturated, while the wetting fluid saturation in the coarser grained regions exhibit low water saturations with most of the water present as films. In Fig. 6(b) we illustrate the network structure of the connected *non-wetting* phase at the same saturation. The non-wetting phase remains strongly connected along the bedding plane with the phase concentrated in the coarser laminations. This strong partitioning of the wetting and non-wetting phases leads to the laminations behaving essentially independently (akin to parallel resistors) and therefore similar values of  $n$  are observed under oil-wet and water-wet conditions parallel to the bedding planes. The laminations also lead to the clear difference in the resistivity index perpendicular to the bedding planes.

### Sucrosic Dolomites

Results for the cementation exponent measured along three orthogonal axes are given in Fig. 5(b). Calculations were performed on  $(1200)^3$  subsamples of the image and measured in three orthogonal directions. No anisotropy was observed. The high porosity sample exhibits  $m=1.8$ , while the intermediate samples both exhibit  $m=2$ . The low porosity sample exhibits a high value of  $m$ . We observe reasonable agreement between the image and experimental data and in both cases observe a strong increase in  $m$  with decreasing  $\phi$ . Focke & Munn, 1987 showed extensive laboratory data for the cementation exponent of sucrosic dolomites with intercrystalline porosity and open textures; in all cases the value of  $m$  was approximately 2. Three of the four samples exhibit this classical behaviour.

We show exemplary data for RI properties in the high and intermediate sucrosic dolomite samples in Fig. 7. We observe very different  $n$  values under water and oil wet conditions. Both samples exhibit  $n=2$  for high and intermediate  $S_w$  and increasing  $n$  at lower  $S_w$ ; no experimental data is currently available on these samples for comparison. The oil wet samples exhibit a much higher value of  $n>5$  for all saturations and  $n$  increasing with

decreasing  $S_w$  in agreement with experiments of Sweeney & Jennings, 1960 for carbonates.

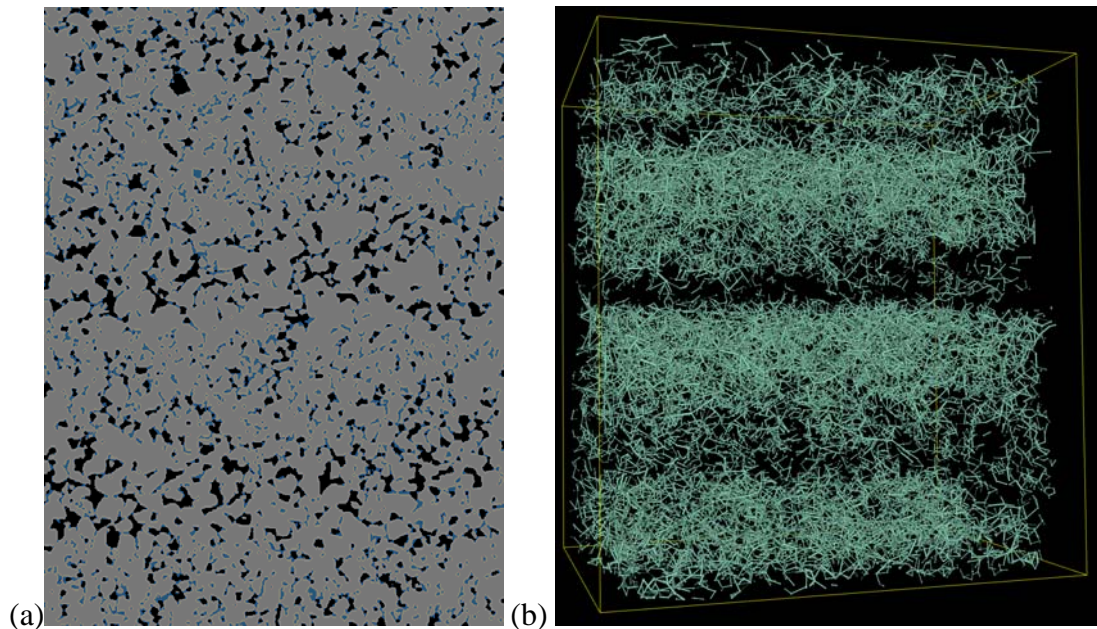


**Figure 6:** (a) 2D slice of clean laminated sand with wetting phase distribution (blue) and wetting phase (black) at  $S_w = 0.42$ . (b) 3D distribution of non-wetting phase the same saturation. Image sizes: (a) 1800 x 1400; (b) 1800 x 1400 x 300.

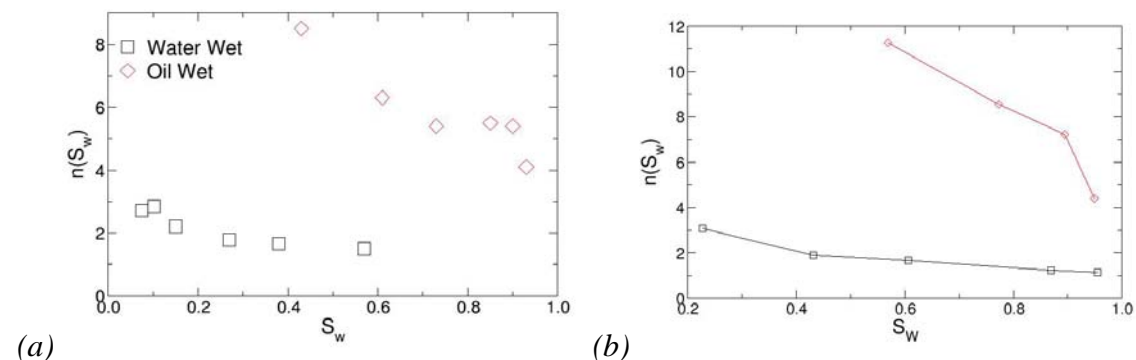


**Figure 7:**  $n(S_w)$  for the (a) high and (b) intermediate porosity homogeneous dolomite samples.

### Model Dual Porosity Carbonates

Resistivity simulations on the fully water saturated sample gives  $m=1.75$  on the dual porosity sample (Fig. 1(e)). The RI data is summarized in Fig. 8. We first compare the water wet drainage simulation data (diamonds) to experiment on sister core material (Padhy et al., 2005, 2006). We note that the simulation gives a slightly smaller value of  $n$ ; the variation may be due to the fact that experiment and simulation are performed on different samples and the natural heterogeneity in the sample. Imbibition RI simulations

exhibits a small degree of hysteresis. Simulation of oil wet drainage exhibits large values of  $n$  as was observed in the clastic samples.

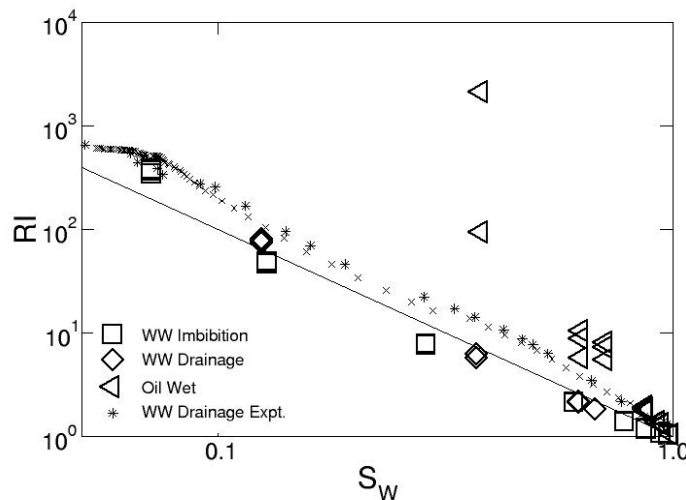


**Figure 8:** *RI under different wettability conditions for the model dual-porosity carbonate sample. Experimental details given in Padhy et al, 2005, 2006.*

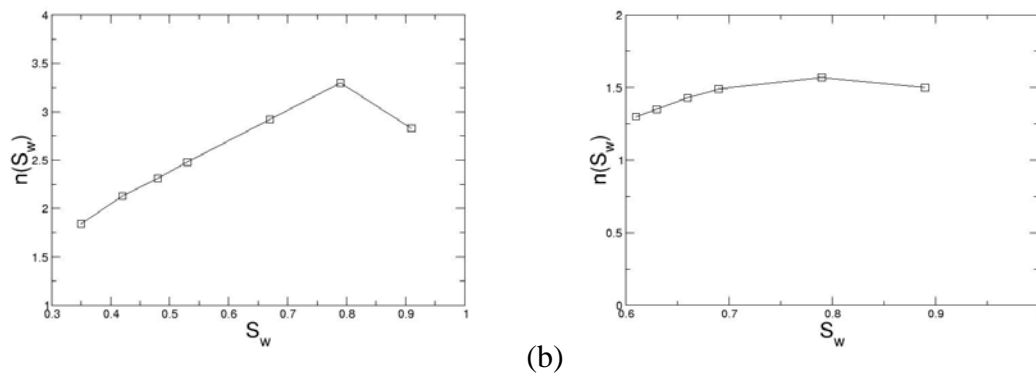
#### Bioclastic Grain/Packstone:

The bioclastic sample exhibits microporosity which cannot be directly resolved but will contribute significantly to the resistivity properties. The microporous phase is primarily made up of skeletal debris; the internal fabric of the microporous phase consists primarily of uniform sized subhedral crystal micrite crystals (Marzouk et al, 1998). The microporous phase therefore is expected to consist of a network of high porosity, highly connected pores with equant pores. This microstructure resembles that observed in the sucrosic dolomite samples which exhibit  $m \sim 2$ . We assign the conductivity of the microporous phase ( $\phi_{\text{micro}}$ ) via Archie's equation;  $\sigma_{\text{micro}} = \phi_{\text{micro}}^2$ . This assignment is also consistent with the work of Focke & Munn, 1987 who found that matrix porosity without any significant moldic, vuggy or fracture porosity consistently exhibits  $m=2$ .

Simulations are then performed on a significant subset of the full image volume ( $1200^3$ ). For sample 11 we observe variation in the value of Archie's exponent with orientation ( $m=2.29, 2.31, 2.45$ ) and a mean value  $m = 2.32$ . For sample 12 we observe stronger variation in the value of Archie's exponent with orientation (2.11, 2.61, 2.34) with a mean  $m = 2.35$ . The value of the cementation exponent of carbonate rocks has been related by Lucia, 1983 to the amount of interparticle porosity, the amount of separate vug porosity and the presence or absence of touching vugs (see Fig. 7 of Lucia, 1983). Lucia argued that the addition of separate vugs to a nonvuggy rock increases porosity but contributes little to the electrical and fluid transport properties of the rock. From the 3D microtomogram we have already partitioned the macropores into two classes; the connected macropores which are connected globally via a macropore network and the separate macroporosity which are connected only through the meso / micropores (non-resolved pores). In sample 11 we observe 8.2% separate macroporosity in a total porosity of 27.2%. This equates to 30% separate macroporosity and, according to Lucia's empirical rule, an expected exponent of  $m=2.3$ . In sample 12 we observe 9% separate or

isolated macroporosity in a total porosity of 23.2%. This equates to 38% separate macroporosity and accordingly a predicted exponent  $m=2.38$ . These predictions compare very well with the result obtained directly from the microtomographic images.

Due to the presence of microporosity in these samples simulations are performed under altered model wettability conditions. In particular we report data for mixed wet conditions which attempt to mimic conditions equivalent to experimental laboratory tests for  $n$  in restored state cores where resolved pores in the tomogram (pores with the *largest* pore throats) are assumed to be oil wet and unresolved porosity (pores with the *smaller* pore throats) are assumed to remain water wet. Here the assumption is that the throat size where pore throats change from oil to water wet is correlated to the image resolution. In reality this will depend on the local capillary pressure. Results for the two samples are shown in Fig. 9. We note non-standard behaviour in the RI curves; the curves exhibit a non-linear trend with  $n$  exhibiting a maximum at intermediate  $S_w$ . Low values of  $n$  are also observed given the oil wet nature of the core material; this low resistivity behaviour is primarily due to the connectivity of the microporous phase. Non standard behaviour in the resistivity of carbonates has been widely reported by Fleury et al., 2004; at this point we do not have experiments on sister core material under identical wettability conditions to test the quality of the predictions from the image data.



(a) (b)  
**Figure 9:** RI under mixed wettability conditions for the complex bioclastic carbonate samples.

## CONCLUSIONS

A 3D pore scale imaging and resistivity study has been undertaken on a range of core material from simply sintered bead packs through to complex microporous carbonates. Archie's cementation exponent  $m$  from image data is in good agreement with experiment when available. Data for the sintered bead pack, the Fontainebleau sands and sucrosic dolomites agree well with experiment over a range of  $\phi$ . We do note a consistent increase in the cementation exponent with decreasing porosity. Simple sintered systems  $\phi=38\%$  give  $m<1.4$ , Fontainebleau sands at 13-17% give  $m=1.8$  and lower porosity samples  $m=2.2$ . This range of  $m$  was reported by (Carothers et al., 1968). We also note an increase

in the cementation exponent for the sucrosic dolomite samples with decreasing porosity in agreement with experiment. The laminated sand sample exhibits only small anisotropy in  $m$ . The value of the cementation exponent of carbonates may be empirically related to the fraction of disconnected macroporosity as described by Lucia, 1983. Drainage RI simulations were undertaken on the sample data. The prediction of the saturation exponent of the Archie-type rocks from image data is in reasonable agreement with experiment where available. Deviations are observed at low water saturation; this is believed to be due to finite image resolution. Under water-wet conditions the drainage RI for most samples exhibited Archie-type behaviour— $n=2$  and constant  $n(S_w)$  for  $S_w > 20\%$ . The behaviour of  $n(S_w)$  under oil-wet drainage conditions exhibits significantly larger values of the saturation exponent  $n > 4$ . The laminated system exhibits strong anisotropy correlated to the bedding axes, but little difference between oil-wet and water-wet  $n$  parallel to the laminations. The dual phase system exhibits classical Archie behaviour and conventional  $m$  and  $n$  despite the complex pore space. The bioclastic sample exhibit values of  $n$  that vary strongly with water saturation.

## ACKNOWLEDGEMENTS

The authors acknowledge the Australian Research Council and member companies of the Digital Core Consortium for their support. We thank Total and Japan Oil Gas and Metals Corporation for permission to present some of the data in this work. We thank the A.N.U. Supercomputing Facility and the Australian Partnership for Advanced Computing for very generous allocations of computer time.

## REFERENCES

1. Arns, C.H., M.A. Knackstedt, E. Garboczi and W.V. Pinczewski (2002): "Computation of linear elastic properties from microtomographic images: Methodology and agreement between theory and experiment." *Geophysics* **67** (5), 1391-1405.
2. Arns, J. Y., A. P. Sheppard, C. H. Arns, M. A. Knackstedt, A. Yelkhovskiy, W. V. Pinczewski (2007): "Pore level validation of representative pore networks obtained from micro-CT images", *Proceedings of the Annual Symposium of the Society of Core Analysts*, SCA2007-A26, Calgary, Canada.
3. Bekri S, Howard J, Muller J, and Adler P.M. "Electrical Resistivity Index in Multiphase Flow through Porous Media", *Transport in Porous Media* (2003) **51**, 41-65.
4. Berkowitz B. and Hansen D.P., "A Numerical Study of the Distribution of Water in Partially Saturated Porous Rock", *Transport in Porous Media*, (2001) **45**, 303-319.
5. Blunt M, Jackson M.D, Piri M, Valvatne Per. H., "Detailed physics, predictive capabilities and macroscopic consequences for pore network models of multiphase flow", *Advances in Water Resources* (2002) **25**, 1069-1089.
6. Carothers, J. E., 1968: "A statistical study of the formation factor relation": *The Log Analyst*, **9**, 13-20.
7. Doyen, P. (1988): "Permeability, Conductivity and pore geometry of sandstone", **93**, 7729-7740.

8. Fleury, M., Efnik, M. and Kalam, Z., (2004), "Evaluation of water saturation from resistivity in a carbonate field; from laboratory to logs: SCA2004-22.
9. Focke J. W. and Munn, D (1987): "Cementation exponents in Middle Eastern carbonate reservoirs: *SPE Formation Evaluation*, **2**, 155-167.
10. Garboczi, E. J. and Day, A. R. (1995): "An algorithm for computing the effective linear elastic properties of heterogeneous materials: 3D results for composites with equal phase Poisson ratios", *J. Mech. Phys. Solids*, **43(9)**, 1349-1362.
11. Ghous, A., Bauget, F., Arns, C.H., Sakellariou, A., Senden, T. J., Sheppard, A. P., Sok, R.M., Pinczewski, W. V., Beck G. F, Harris, R. G. and Knackstedt, M. A. (2005): "Resistivity and permeability anisotropy in laminated sands via digital core analysis", *Proceedings of the SPWLA 46<sup>th</sup> Annual Logging Symposium*, Paper VVV, New Orleans, USA.
12. Jacquin, C. G. (1964): "Correlation entre la permeabilite et les caracteristiques geometriques du gres de Fontainebleau", *Revue Inst. fr. Petrole*, **19**, 921.
13. Knackstedt, M. A., Arns, C. H., A. Ghous, A. Sakellariou, T. J. Senden, A. P. Sheppard, R. M. Sok, W. V. Pinczewski, G. Padhy and M. A. Ioannidis (2006): "3D imaging and flow characterization of pore space of carbonate core samples", *Proceedings of the Annual Symposium of the Society of Core Analysts*, SCA2006-23, Trondheim, Norway.
14. Lucia, F. (1983): "Petrophysical parameters estimated from visual descriptions of carbonate rocks: A field classification of carbonate pore space", *Journal of Petroleum Technology*, **35**, 629-637.
15. Man H.N. and Jing X.D., "Network modelling of mixed wettability on electrical resistivity, capillary pressure and wettability indices", *Journal of Petroleum Science and Engineering* (2002) **33**, 101-122.
16. Marzouk I, H. Takezaki and M. Miwa, Geological Controls on wettability of Carbonate reservoirs, Abu Dhabi, U.A.E.,", *SPE* 29883.
17. Padhy, G., M. A. Ioannidis, C. Lemaire and Coniglio, M. (2006): "Measurement and interpretation of non-Archie Resistivity behavior in model and real vuggy carbonates", *Proceedings of the Annual Symposium of the Society of Core Analysts*, SCA2006-11, Trondheim, Norway.
18. Sakellariou, A., T.J. Senden, T.J. Sawkins, M.A. Knackstedt, A. Limaye, C.H. Arns, A.P. Sheppard, and R.M. Sok (2004): "An x-ray tomography facility for a wide range of mesoscale physics applications." U. Bonse (ed.): *Proceedings of SPIE* **5535**. Bellingham, WA, pp. 166-171
19. Sakellariou, A., T. J. Sawkins, T. J. Senden and A. Limaye (2004a): "X-ray tomography for mesoscale physics applications", *Physica A*, **339**, 152-158.
20. Sharma, M. M., Garrouch, A. and Dunlap, H. F. (1991), "Effect of wettability, pore geometry and stress on electrical conduction in fluid-saturated rocks", *The Log Analyst*, **32**, 511-526.
21. Sheppard, A. P., R. M. Sok and H. Averdunk (2004): "Techniques for image enhancement and segmentation of tomographic images of porous materials", *Physica A*, **339**, 145-151.
22. Sok, R. M., Arns, C. H., Knackstedt, M. A., Sheppard, A. P., Senden, T.J., Pinczewski W.V. and Okabe, H. (2007), "Estimation of petrophysical parameters from 3D images of carbonate core", *Proceedings of the SPWLA 1<sup>st</sup> Annual Middle Eastern Regional Symposium*, Paper A, Abu Dhabi, UAE.
23. Sweeney, S. A. and Jennings, H. Y. (1960), "Effect of wettability on the electrical resistivity of carbonate rock from a petroleum reservoir", *J. Phys. Chem.*, **64**, 551-553.
24. Toumelin, E, Torres-Verdin, C., Davarajan, S and Sun, B. (2006): "An integrated pore scale approach for the simulation of grain morphology, wettability and saturation history effects on electrical resistivity and NMR measurements of saturated rocks", *Proceedings of the Annual Symposium of the Society of Core Analysts*, SCA2006-20, Trondheim, Norway.